THE ASTROPHYSICAL JOURNAL, 423:553–565, 1994 March 10

X-RAY EMISSION FROM A SIMULATED CLUSTER OF GALAXIES

JOHN C. TSAI,[1,2] NEAL KATZ,[1] AND EDMUND BERTSCHINGER[1]
Received 1993 June 4; accepted 1993 September 20

ABSTRACT

Using the 1993 cluster simulation of Katz & White, we analyze the intracluster medium and investigate the accuracy of the standard hydrostatic method for determining cluster masses. We show that the simulated cluster gas is in hydrostatic equilibrium with a subsonic flow toward the center. Inside a radius of ~ 100 kpc, this flow is in a steady state. The cooling time is shorter than a Hubble time within the central 50 kpc. The flow rate is regulated by the gas sink in the middle of the cluster and the PdV work done as the gas flows in, verifying the standard cooling flow scenario. We simulate observations of the cluster using the instrument parameters of the *EXOSAT* ME detector and the *Einstein* IPC detector. Even though the intracluster gas is not isothermal, isothermal models of the cluster, excluding regions within 100 kpc of galaxies, fit the *EXOSAT* X-ray spectra as well as they fit real clusters. The X-ray surface brightness distribution is similar to that of real clusters, again excluding the galaxies. We simulate the procedure used to determine the masses of real clusters. We use the equation of hydrostatic equilibrium together with the temperature derived from an isothermal fit to the simulated *EXOSAT* spectrum and the density profile derived from a fit to the simulated IPC surface brightness profile to determine the mass. A comparison of the derived mass profile to the actual mass profile shows that errors of a factor of 2 are possible. If the actual temperature profile is used, the cluster mass is found to an accuracy of better than 25% within the virial radius.

Subject headings: cooling flows — galaxies: clustering — hydrodynamics — intergalactic medium — X-rays: galaxies

1. INTRODUCTION

During the past decade, much progress has been made using cosmological N-body simulations to assess the viability of theories for the formation of galaxies and structure in the universe (e.g., Gelb 1992; Bertschinger 1993; Ostriker 1993 and references therein). However, because these types of simulations do not include the effects of gas dynamics, their use is limited. The comparisons with observations are generally restricted to scales larger than those of galaxies or perhaps clusters of galaxies. The recent development of techniques that can simultaneously evolve not only the dissipationless dark matter component but also a dissipational gaseous component allows a more detailed comparison to be made with the observations (Evrard 1990; Katz & Gunn 1991; Cen & Ostriker 1992; Katz, Hernquist, & Weinberg 1992; Evrard, Summers, & Davis 1994). For example, Evrard (1990) studied the evolution of a Coma-sized cluster and calculated the expected Sunyaev-Zel'dovich decrement. More recently, Katz & White (1993) found that the abundance of cool lumps ("galaxies") in their simulated cluster is consistent with the observed number of galaxies, although they could only resolve the most massive "galaxies." Thus inclusion of gas dynamics may solve the overmerging problem that is ubiquitous in pure N-body simulations.

In addition to issues related to the formation of the galaxies themselves, hydrodynamical simulations also enable study of the properties and evolution of the intracluster gas (Evrard 1990; Thomas & Couchman 1992; Katz & White 1993). These studies are not only important for understanding the intrinsic properties of the gas itself, but also for assessing the validity of cluster mass estimates obtained using the gas as a tracer of the gravitational potential. Because the total mass, gas density, and gas temperature are explicitly known in a simulated cluster, it provides a realistic arena for testing the accuracy of the various deprojection techniques used to determine these properties in real clusters. Furthermore, the strong thermal X-ray emission from clusters has resulted in a wealth of data from various X-ray satellites that can be compared with simulated clusters to test the viability of various cosmological theories of cluster formation.

In this paper we pursue several of these lines of investigation. For this purpose we use the simulation of Katz & White (1993, hereafter KW) that models the formation and evolution of a $2 \times 10^{14}\ M_{\odot}$ cluster within a flat cold dark matter cosmogony (CDM) with a dark matter to baryonic matter mass ratio of 10 to 1 and an amplitude corresponding to a linear bias factor of 2.6. The simulation uses smoothed particle hydrodynamics (SPH) to treat the hydrodynamics and a hierarchical tree code to treat the gravity (Hernquist & Katz 1989; Katz & Gunn 1991). The spatial resolution is 20 kpc, and the effects of both radiative and Compton cooling are included. Also, the simulation uses a multigrid technique that enables the simulation to model correctly the gravitational effects on the cluster arising from a volume much larger than the cluster itself. This technique ensures that the cluster forms and evolves within the proper large-scale gravitational field and that the cluster potential does not begin to dominate the entire simulation volume. These are all improvements on previous cluster simulations (e.g., Evrard 1990; Thomas & Couchman 1992). The interested reader can refer to KW for further details about the simulation itself.

An initial analysis of the properties of the intracluster gas in the simulation and a comparison with some existing X-ray data have already been performed by KW. They find that the cluster has a nonisothermal temperature profile and that the X-ray surface brightness profile is consistent with the observed

[1] Department of Physics, MIT 6-207, Cambridge, MA 02139.
[2] NASA/Ames Research Center, Mail Stop 245-3, Moffett Field, CA 94035-1000.

profile of the Virgo cluster outside the central region. Beyond these conclusions, however, little further analysis of the intracluster gas or further comparison to observed clusters was performed. It is therefore unclear whether the surface brightness profile of the simulated cluster is consistent with any cluster other than Virgo or whether the nonisothermal nature of the gas is consistent with actual temperature profiles. The temperature profile of the gas around M87 is nearly isothermal (Tsai 1993, 1994), in apparent disagreement with the profile of the simulated cluster.

We will begin our present study by expanding on the discussion of KW and by making a more detailed comparison of the simulation to observed clusters. We simulate observations of the cluster using the instrumental parameters of the Medium Energy (ME) detector (Argon proportional counters) on board the *EXOSAT* satellite (for a description of the instrument, see Edge 1989). These simulated spectra are used in the same manner as *EXOSAT* observations of real clusters would be used. We also make simulated observations of the cluster using the instrumental parameters of the Imaging Proportional Counter (IPC) on board the *Einstein* satellite (Giacconi et al. 1979) to produce X-ray surface brightness profiles. We compare these simulated observations with actual data from comparably massive clusters as a test of the cold dark matter theory. Since we can "observe" only the one cluster simulated by KW, we cannot test whether the theory produces a distribution of clusters that agrees with the observations. Such a test was attempted by Frenk et al. (1990) using purely dissipationless simulations. However, we hope to develop a better understanding of the physical processes that are of primary importance in cluster evolution since the effects of gas dynamics are included in the KW cluster simulation. Our methods of comparison with the observations constitutes an improvement over previous work since we compare actual observed quantities instead of physical properties that are several steps removed from the actual observations by a series of deconvolutions.

Having "observed" our cluster with *EXOSAT* and the IPC, we test the accuracy of the standard method for determining the total mass of a cluster using X-ray observations. In this method, the intracluster gas is assumed to be isothermal and in hydrostatic equilibrium. Under the assumption of isothermality, the X-ray surface brightness profile is easily deprojected to yield the gas density profile, and the mass profile is then determined by applying the equation of hydrostatic equilibrium (Fabricant, Lecar, & Gorenstein 1980; Fabricant & Gorenstein 1983; Jones & Forman 1984). We mimic this method of determining the mass profile for the KW cluster by using the temperature obtained by an isothermal fit to the simulated *EXOSAT* data and a density profile derived from the simulated IPC data. A comparison of the mass profile derived in this manner with the actual mass profile of the KW cluster indicates the accuracy of the method and, in the case of poor agreement, allows us to determine the reasons for the disparity.

Deriving the mass profile from X-ray emission is only one of several methods used to determine the masses of clusters. Another method treats the galaxies as test particles in the cluster gravitational potential field and estimates the mass using some variant of the virial theorem (e.g., Heisler, Tremaine, & Bahcall 1985). The X-ray method has several advantages over the virial method. The statistical accuracy of the X-ray method is not limited by the number of galaxies in the cluster. Furthermore, the mass can be derived as a function of radius whereas the virial method only gives a general estimate of the cluster mass. Cluster masses can also be estimated using gravitational lensing provided there are enough background sources to trace out the cluster potential. The many faint blue background galaxies discovered by Tyson and collaborators (Tyson et al. 1984; Tyson, Valdes, & Wenk 1990) occur in sufficient numbers to act as these background sources and have been observed to be lensed by several clusters (Tyson 1991). However, most cluster masses are currently determined using either the X-ray or virial method. Therefore, a better understanding of the uncertainties in determining cluster masses using X-ray observations is very important not only to better understand the clusters themselves but also for cosmology in general, since estimates of the total mass density of the universe often rely on cluster masses.

Finally, we note several other relevant issues that we are unable to address owing to various limitations of the KW simulation. Because the KW simulation resolves only the largest galaxies, there are only ~ 4 galaxies in the final cluster. This small number of galaxies makes it impossible to address the "β problem" fully (see § 4). Also, since KW simulated only one cluster we are unable to study the statistical properties of clusters, for example, the correlation between X-ray emission and the optical galaxy distribution. Because the central region of the KW cluster is not well modeled for reasons that we discuss below, we are unable to study any issues that rely on the conditions at small radii. For example, it is not possible to test the detailed modeling of the central regions of clusters, as in Tsai (1993, 1994) for the gas around M87. Finally, it is not practical to determine the total X-ray luminosity of the KW cluster owing to the unrealistic copious amount of X-ray emission present in the poorly modeled central region.

In § 2 we discuss the physical state of the intracluster gas. We compare our simulated X-ray observation of the KW cluster to real clusters in § 3, and in § 4 we test the accuracy of the standard methods for determining cluster masses. Finally, in § 5 we summarize our conclusions. In the remainder of this paper, we assume a Hubble constant of 50 km s^{-1} Mpc^{-1}.

2. THE NATURE OF THE INTRACLUSTER GAS

First, we summarize the findings of KW concerning the intracluster gas. Figure 1 shows a simulated IPC observation of the KW cluster. The contours represent X-ray flux in an energy range from ~ 0.2 to 4.0 keV and are logarithmically spaced. We place the cluster at a distance of 100 Mpc and project along the x-axis as defined by KW. At this distance 1′ corresponds to 29.1 kpc. As noted by KW, the cluster is not spherically symmetric. The isophotes are somewhat elliptical with axis ratios of ~ 0.7. KW show that the distribution of the gas in the simulation is more spherical than that of the dark matter. Since the simulation resolves only the largest few galaxies, we are unable to comment on the relation of the galaxy distribution to either the gas or dark matter distributions. Buote & Canizares (1992) find that the dark matter distribution is rounder than the galaxy distribution in observed clusters.

The large amount of emission within the inner 3′ region is obvious in Figure 1. This extreme amount of emission is not observed in real clusters as discussed by KW. We elaborate on this discussion below by plotting the IPC surface brightness profile and comparing it to observed clusters. For this comparison, we use the observations of Jones & Forman (1984)

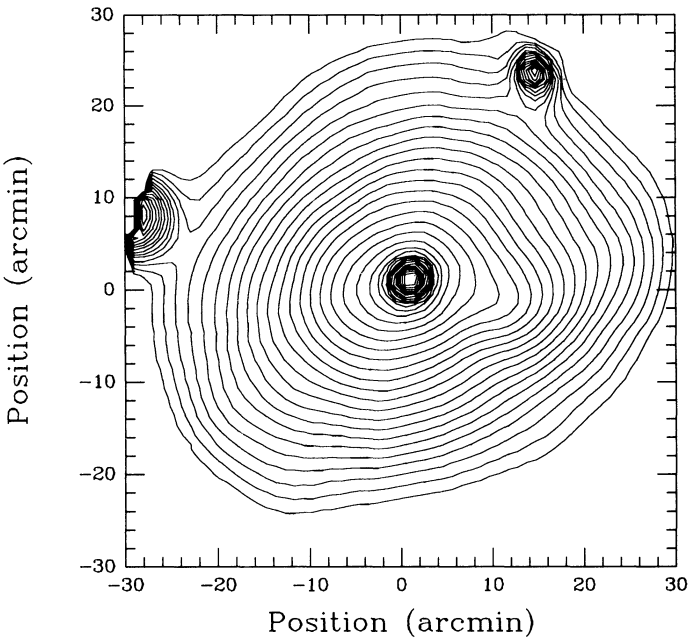

FIG. 1.—Contour plot of the IPC X-ray surface brightness for the simulated cluster. The outermost contour level is 3×10^{-5} IPC counts s^{-1} arcmin^{-2}, and the contour levels are spaced by a factor of 1.3. The count rate is the sum of counts in PHA channels 2 through 9 and corresponds roughly to the energy range 0.2–4.0 keV. The assumed distance is 100 Mpc so that 1′ corresponds to 29.1 kpc.

who divide clusters into two classes: those that have central galaxies located at the X-ray peaks (XD clusters), and those that do not have central galaxies located at the X-ray peaks (nXD clusters). The nXD clusters have X-ray surface brightness profiles that are well fitted by isothermal "β"-models (Cavaliere & Fusco-Femiano 1976) at all observed radii. The XD clusters only fit these models outside their core radius and have surface brightness profiles that are in excess of the "β"-models within their core radius. Since the KW cluster has a central galaxy, we classify it as an XD cluster and restrict our comparisons to observed XD clusters.

KW attribute the unrealistic central X-ray cusp to the lack of star formation in their simulation. As the cluster evolves, dynamical friction drags galaxies towards the center of the cluster where they merge with the central galaxy. Since the galaxies in the simulation are entirely gaseous when they merge, all the orbital energy is quickly radiated away. The net effect of the process is to unrealistically deepen the central potential well. Intracluster gas is drawn into this deep potential where it becomes very hot and dense; producing the copious X-ray emission seen in the center of Figure 1. If the galaxies were mostly stellar when they merged, a major portion of the orbital energy would have gone into the internal velocity dispersion of the stars in the central galaxy. This would limit the central depth of the potential well and presumably eliminate the spurious X-ray emission. Because of the problems with the central region of the cluster, we restrict our attention to regions outside 100 kpc (3′.4) in subsequent discussions. Similarly, the spurious emission from two of the galaxies contaminates the IPC surface brightness profile outside ~24′.

Most theoretical work on cooling flows models the intracluster medium as an ideal gas in hydrostatic equilibrium and assumes that gas flow occurs in a steady state fashion (see, for example, Sarazin 1988). It is interesting to check whether the KW cluster has these properties. For gas in hydrostatic equilibrium, we expect the velocity-dependent terms in the Euler equation to be negligible relative to the pressure and gravity terms. We use the temperature, density, velocity, and mass profiles measured from the simulated cluster to evaluate each of the terms in the radial component of the Euler equation,

$$\frac{\partial v}{\partial t} + v\frac{\partial v}{\partial r} = -\frac{1}{\rho}\frac{\partial P}{\partial r} - \frac{GM(r)}{r^2}, \quad (1)$$

where v is the (radial) velocity, P is the pressure, $M(r)$ is the total mass contained within radius r, and ρ is the gas density. We plot these terms as a function of radius in Figure 2. Note that we use spherical averages for the fluid variables and that we ignore terms involving the tangential velocity, which are significant only at small radius. From Figure 2 we see that the magnitudes of the velocity terms are negligible compared with the pressure and gravity terms implying that the gas is in hydrostatic equilibrium. We should be cautious in this conclusion since it is possible that large streaming motions in the gas may not show up in Figure 2 because spherically averaged fluid variables were used to evaluate the terms in equation (1). However, the close balance of pressure and gravitational forces implies that nonspherical motions are not dynamically important at the radii shown. The subsequent use of the assumption of spherical hydrostatic equilibrium to evaluate the mass distribution (§ 4) should be correct.

We plot several physical properties of the intracluster gas as a function of radius in Figures 3*a*–3*c* at two different times. The solid lines correspond to $z = 0.13$, and the dotted lines to $z = 0.25$. All these quantities are spherically averaged. Figure 3*a* shows the mass-weighted temperature profile of the intracluster gas. The enormous cooling rate is responsible for the extremely rapid drop off in temperature in the central regions of the cluster. The other temperature dips are not due to intracluster gas. When a galaxy falls within a spherical bin, its cold gas causes the dips in the temperature profile seen at logarithmic radii of about -1.0 when $z = 0.25$ and at -0.1 and 0.1 Mpc when $z = 0.13$. Similar bumps occur in Figures 3*b* and 3*c*. The intracluster gas is not isothermal with the temperature dropping by over a factor of 3 from a radius of 100 kpc to a radius of 1 Mpc.

We plot the total number density of the gas, as opposed to the electron or hydrogen atom number density, versus logarithmic radius in Figure 3*b*. The large peak in the central region is again unrealistic. Otherwise, the density profile follows a power law beyond a few hundred kpc and bends over to become relatively flat at smaller radii. This resembles the standard form of the density in isothermal "β"-models (Cavaliere & Fusco-Femiano 1976) where

$$n(r) = n_0\left[1 + \left(\frac{r}{a}\right)^2\right]^{-3\beta/2} \quad (2)$$

and suggests that we should also use these models when making fits to our simulated IPC surface brightness observations. Note the similarity in the shape of the KW density profile to those deconvolved from observed clusters (e.g., Kriss, Cioffi, & Canizares 1983) (we defer further comparisons to § 3).

In Figure 3*c* we plot the radial component of the gas velocity versus logarithmic radius. Within 1 Mpc, the approximate virial radius of the cluster, and outside 100 kpc the velocities range from ~ -40 to -100 km s^{-1} with negative velocity indicating that the gas is flowing toward the center of the

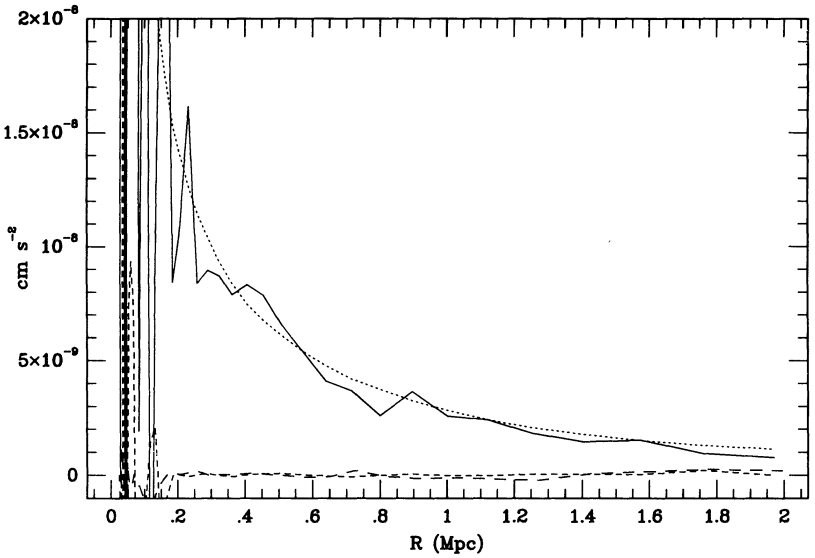

FIG. 2.—Spherically averaged values of the terms in the Euler equation (see eq. [1] in the text). The solid line corresponds to the pressure term, and the dotted line corresponds to the gravitational term. The dashed lines correspond to the velocity-dependent terms: the long dashed line corresponds to the time derivative of the velocity term, and the short dashed line corresponds to the advective term with the radial derivative of the velocity.

cluster. (Note that the larger positive velocity at ~ 100 kpc at $z = 0.25$ is due to a moving galaxy and does not characterize the motion of the intracluster gas.) Since the local sound speed is ~ 700 km s^{-1}, the flow is subsonic. This is consistent with the standard assumptions of the cooling flow hypothesis. We therefore show that an ab initio calculation of cluster evolution within the proper cosmological context naturally gives rise to a subsonic flow of gas toward the center of the cluster. We can further compute the mass accretion rate $\dot{M} = 4\pi r^2 \rho v$ where r is the radius, ρ is the mass density, and v is the radial velocity. The rate is essentially constant inside of ~ 300 kpc at ~ 600 $M_\odot$ yr^{-1}. This rate is comparable with some observed values (e.g., Fabian, Nulsen, & Canizares 1984; Arnaud 1988) although our simulated cluster is on the small side and such large mass accretion rates are usually associated with larger cooling flow clusters. This difference probably reflects the extreme and unrealistically large amount of cooling that occurs in the central regions of the simulated cluster because of the absence of star formation.

To quantify our discussion of the evolution of the gas, we plot several important timescales in Figure 4. These are evaluated at $z = 0.13$. Since the flow is dominated by the processes that occur on the shortest timescales, such a plot not only indicates whether flow is in a steady state but also what processes dominate the evolution of the intracluster gas. In Figure 4 the light solid line represents the cooling time

$$t_{\rm cool} = \frac{3}{2}\frac{nkT}{n_e n_{\rm H}\Lambda(T)}, \tag{3}$$

where n is the total gas density, n_e and $n_{\rm H}$ are the densities of electrons and hydrogen atoms, respectively, and $\Lambda(T)$ is the bolometric emissivity of the hot gas in units of ergs cm^3 s^{-1}. Note that with this definition we have not included the effects of the compressional work done on the gas by the pressure. If we had, we would simply replace the internal energy density by the enthalpy $[(5/2)nkT]$ in the numerator of equation (3). The horizontal dotted line in the figure shows the approximate lifetime of the cluster ($\sim 1.09 \times 10^{10}$ yr).

At all radii except for the very center of the cluster, the cooling time is longer than the lifetime of the cluster. Therefore, local cooling plays an insignificant role in the evolution of this cluster. This is consistent with what we know about the gas around M87 where the cooling radius, defined to be the radius where the cooling time equals the lifetime of the cluster, is ~ 70–90 kpc (Stewart et al. 1984; Bertschinger 1989). The enormous X-ray emission in the central region, as mentioned above, results in the very rapid drop in the cooling time toward the center of the cluster.

The flow time, defined to be the radius divided by the radial component of the gas velocity, measures the significance of the flow itself and is plotted as the dark solid line in Figure 4. A significant inflow occurs for radii less than about 400 kpc. It is interesting to compare this timescale to the timescales that characterize the time variability of the fluid variables. We compute two such "time derivative" timescales: the density timescale, defined to be

$$t_n = \left(\frac{d\ln n}{dt}\right)^{-1}, \tag{4}$$

plotted as the short dash-dotted line in Figure 4, and the velocity timescale, defined by

$$t_v = \left(\frac{d\ln v}{dt}\right)^{-1}, \tag{5}$$

plotted as the long dashed-dotted line. In the outer region where the flow is significant, from ~ 100 to 400 kpc, the "time derivative" timescales are comparable to the flow time indicating that the flow can change appreciably during the lifetime of the cluster at these radii. Inside about 80 kpc, however, the "time derivative" timescales both become longer than the flow time by about a factor of 10. Therefore, although the flow may change somewhat during the lifetime of the cluster, assuming that the gas is in a steady state is a good approximation since the time dependent terms are about 10 times less important than the terms giving the general advection of the gas.

The relevance of this conclusion to the investigation of

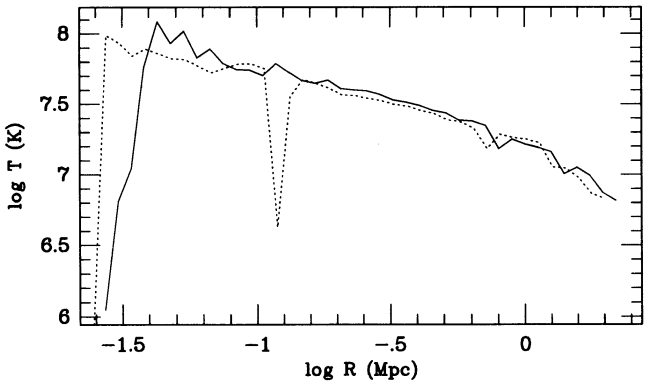

FIG. 3a

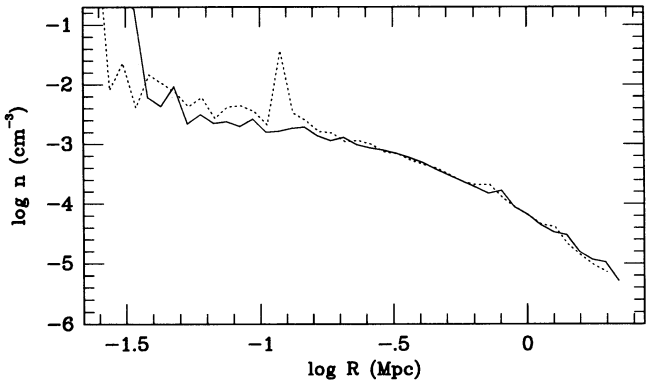

FIG. 3b

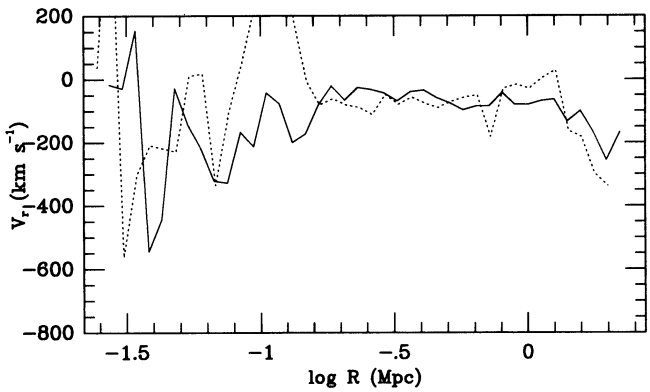

FIG. 3c

FIG. 3.—(*a*) Mass-weighted, spherically averaged temperature of the cluster gas plotted *vs.* radius. The solid line corresponds to $z = 0.13$, and the dotted line corresponds to $z = 0.25$. (*b*) Spherically averaged gas number density plotted versus radius. The solid line corresponds to $z = 0.13$ and the dotted line corresponds to $z = 0.25$. (*c*) Spherically averaged radial component of the gas velocity plotted versus radius. The solid line corresponds to $z = 0.13$ and the dotted line corresponds to $z = 0.25$.

cooling flows is clear. It is generally assumed that within the cooling radius the flow is in a steady state. Here, we have demonstrated the steady state nature of the flow within the cooling radius arises quite naturally in a simulated cluster, again lending support to the standard cooling flow picture.

To extend the above arguments and to understand the exact cause of the gas flow inside the cooling radius, we consider two additional timescales. First, we consider the dynamical time, which characterizes the flow due to gravity and which we define to be

$$t_{\rm dyn} = \sqrt{\frac{r^3}{GM(r)}}, \tag{6}$$

and the sound crossing time, which is just the radius divided by the local sound speed. The short dashed line in Figure 4 plots the dynamical time and the long dashed line plots the sound crossing time. As defined, hydrostatic equilibrium does not imply that the sound crossing time should be equal to the dynamical time, rather

$$\left(\frac{t_{\rm sound}}{t_{\rm dyn}}\right)^2 = -\left(\frac{d\log n}{d\log r}\right). \tag{7}$$

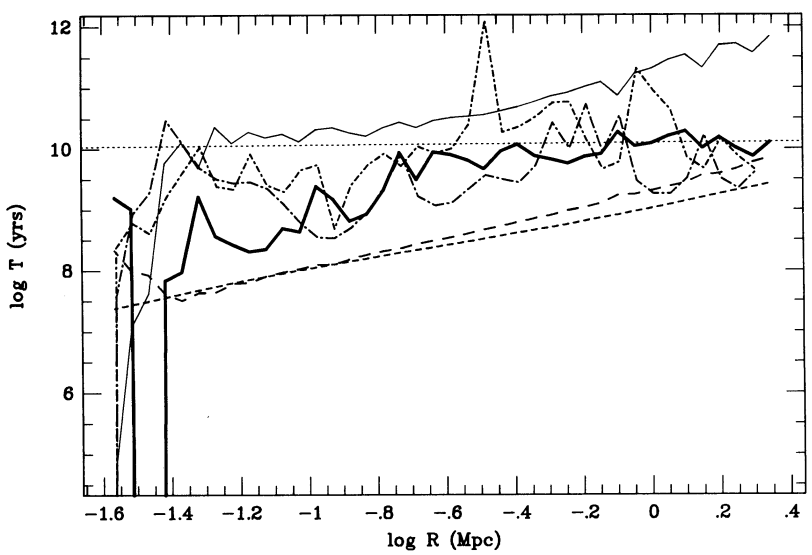

FIG. 4.—Cluster timescales as a function of radius (see the text). The horizontal dotted line indicates the Hubble time of 1.09×10^{10} yr. The light solid line corresponds to the cooling time. The dark solid line corresponds to the flow time. The short dashed-dotted line corresponds to the density timescale, and the long dashed-dotted line corresponds to the velocity timescale. The dynamical timescale is represented by the short dashed line, and the sound crossing time is represented by the long dashed line.

From Figure 3*b*, we can see that the slope of the density profile becomes more negative with increasing radius. Therefore, hydrostatic equilibrium would imply that the dynamical time should get shorter than the sound crossing time as the radius increases, just as it does in Figure 4.

Why does the gas flow in the simulation have the properties described above? The answer lies in the rapid cooling of the central region of the cluster, illustrated by the precipitous drop in the cooling time. We have analyzed the Euler equation above to establish the existence of hydrostatic equilibrium, but the fluid must also satisfy the energy equation and the continuity equation. The energy equation simply requires that the energy lost by the central region as it cools must be replenished. Since conduction is not included in the simulation, the only way to accomplish this is by the advection of hotter gas from outside the cluster core, creating a flow of gas toward the center of the cluster. The continuity equation then simply accommodates this flow. The gas flows subsonically because the rate at which gas is required to carry heat into the center is small, making the gas velocities small. Note that this interpretation applies only in the central region, that is, within 100 kpc, where we demonstrated that a steady state flow is a good assumption.

In summary, we have a realization on the computer of what would be considered a typical cooling flow cluster in a steady state and in hydrostatic equilibrium. From the standpoint of the physics included in the simulation, the present state of the intracluster gas arises from a generic set of evolutionary processes that are easy to understand. This, of course, does not necessarily imply that the simulated cluster is similar to real clusters (this question will be investigated in the next section), but it does mean that the present state of the gas is comprehensible. The final state of the gas coincides with assumptions that are typically made when real clusters are modeled, which is encouraging for cluster analysts.

We end with a discussion of the relative distributions of the gas and dark matter in the simulation. Cumulative mass profiles are plotted in Figure 5. Although a pure power law does not appear to be the best fit to these profiles, the logarithmic slope is close to unity, similar to what is found for M87 (Tsai 1993, 1994). This fact, along with the similarity of the density profiles to observed profiles, suggests that at least certain characteristics of real clusters are being captured in the simulation.

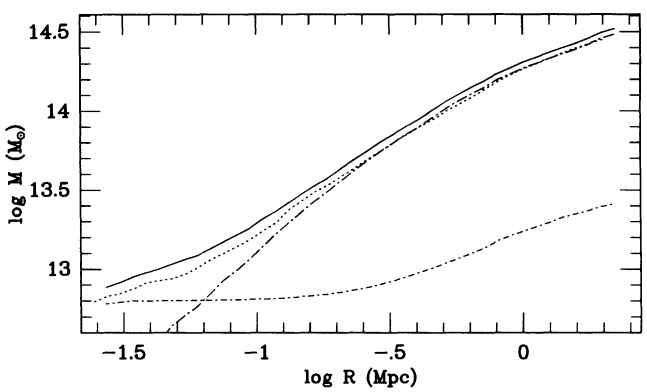

FIG. 5.—Total mass contained within a given radius plotted vs. radius. The solid line corresponds to $z = 0.13$, and the dotted line corresponds to $z = 0.25$. The long dashed-dotted line corresponds to just the dark matter mass, and the short dashed-dotted line corresponds to just the gas mass, both at $z = 0.13$.

The cumulative mass profile of the dark matter component for $z = 0.13$ is plotted as the dotted-long dashed line and that of the gas is plotted as the dotted-short dashed line. At small radii, the gas component dominates the total mass, while at larger radii the dark matter component dominates. This behavior is easily understood. At large radii, the mass ratio should be about 10 to 1 since this is the assumed global mass ratio in the simulation. At small radii, the gas component dominates the total mass because of the strong central cooling flow as well as a combination of dynamical friction and tidal stripping. The interested reader can refer to KW for a detailed discussion of the evolutionary processes in the cluster simulation.

Finally, we note that the simulated cluster is fairly well described by a polytropic model with a polytropic index of about 4/3 between 100 kpc and 1 Mpc. The specific entropy increases outward making the gas convectively stable. This behavior has been noted, when thermal conduction is not included, since the early work of Perrenod (1978).

3. COMPARISON TO REAL CLUSTERS

To generate the simulated *EXOSAT* and IPC observations, we place the cluster at a distance of 100 Mpc to minimize the limitations of the simulation. The cluster could not be placed too close or the unrealistically bright center would dominate the X-ray emission. For example, if we were to place the cluster at a distance of 15 Mpc, the approximate distance to M87, the central cusp of emission would subtend 16′. Since the useful outer extent of the IPC is 30′, only the data from 16′ to 30′ could be used to compare with actual observations. Placed at 100 Mpc, the central region lies within 3′ of the center. Because the IPC point response of ∼1.′5 has not been deconvolved from real observations (Fabricant & Gorenstein 1983), the data from this central region are not useful for comparisons in any case. The same considerations apply for the *EXOSAT* observations. Since the *EXOSAT* transmission function peaks at the center and falls almost linearly with radius (FWHM ∼45′, see Edge 1989), a central excess within 16′ would significantly affect the emission observed by the instrument. Placed at 100 Mpc, the effect of the center is much less significant.

The strong cusp of emission in the center of the simulated cluster prevents us from considering instruments such as the *Einstein Observatory* Focal Point Crystal Spectrometer (FPCS) and Solid State Spectrometer (SSS). In both cases, the small fields of these instruments (3′ × 30′ for the FPCS and 6′ diameter for the SSS) imply that the emission from the central 3′ would dominate the observed count rates. In contrast, the *EXOSAT* ME has a field of more than 45′. The *Einstein Observatory* High Resolution Imager (HRI) also primarily observed the central regions of clusters. Therefore, the data available from this instrument cannot be compared to simulated observations of our cluster.

In an effort to remove the unrealistic aspects of the simulated cluster, we consider three different cases when making our simulated *EXOSAT* observations. In the first case, we just compute the spectrum using the entire cluster, including all projected material and make the subsequent analysis based on that data. In the second case, we ignore the central 70 kpc (in three dimensions) and compute the emission only from the gas outside this radius in an attempt to remove the unrealistic core region. Finally, in the third case, we attempt to remove all the unrealistic regions of the simulated cluster. We exclude the regions within 100 kpc of the center and those within 100 kpc

of the two largest galaxies. In these regions the lack of star formation in the simulation causes unrealistic X-ray cusps. We also restrict ourselves to the central 1.8 Mpc, approximately twice the virial radius. We do this to remove the emission from a small group that appears in projection. Even though it just simply ignores the parts of the cluster simulation that are incorrectly modeled, we feel it is most appropriate to compare this last case to actual observations. We only study the first two cases to assess the effects of these regions. In the simulated IPC observations the core does not present a problem since we exclude this region from the fitting process.

We compute the X-ray emission in the energy bands appropriate to the two instruments, 128 energy bands for the *EXOSAT* and 150 for the IPC, using a method consistent with the SPH formalism. In effect, we compute the emission for each of the SPH particles and then project it along the line of sight (see § 6 of KW for details). This produces a two-dimensional map of the flux per unit solid angle for each of the energy bands that are observed by the instruments. We bin this two-dimensional map into pixels 1′ on a side. When computing the X-ray emission, we use the atomic emissivities of Raymond (1989) assuming half solar abundances for all elements heavier than helium and solar abundances for hydrogen and helium. These abundances are consistent with the measured values from real clusters (Mushotzky 1984; Edge, Stewart, & Smith 1988; Koyama, Takano, & Tawara 1991). We further assume that the gas is in ionization equilibrium, which should be valid for the temperatures and densities under consideration (Edgar & Chevalier 1986; Canizares, Markert, & Donahue 1988).

We convert the X-ray emission in each of the pixels into instrument counts in an instrument-specific manner. First, we assume that the fields of both instruments are centered on the peak of the X-ray emission. For the *EXOSAT* observations, we multiply the X-ray spectrum from each pixel by the transmission function appropriate for the location of that pixel to derive the spectrum incident on the detector. The transmission function measures the fraction of the flux incident on the *EXOSAT* collimator at a given location that reaches the detector. Therefore, it is a function of the location of the pixel relative to the field of view. We convolve the spectrum with the instrument response function to generate the instrument count rate spectrum, that is, the count rate in each of the instrument pulse height analyzer (PHA) channels. Then we sum together the count rate spectra from each of the pixels in the *EXOSAT* field to get the total *EXOSAT* count rate spectrum for the cluster. Finally, we add Poisson noise to the data assuming that the cluster is observed for 56,620 s, the duration of one of the M87 pointings, to get the total number of counts in each PHA channel. We generate a new number of counts for each PHA channel using a Poisson random number generator. We derive the new count rate by dividing the new total number of counts by the assumed observation time. We assume that the errors are caused only by counting statistics and do not include any additional errors present in the real data caused either by background subtraction or instrumental effects.

When making the simulated IPC observations, as with the *EXOSAT* observations, we first take the spectra from each of the pixels and convolve it with the instrument response function to get the instrument count rate spectrum for each pixel. Unlike *EXOSAT*, the IPC has 15 PHA channels. For each pixel, we sum the count rate in channels 2 through 9, approximately the energy range from 0.2 to 4 keV, producing a two-dimensional map of the IPC count rate. Since the IPC point response is $\sim 1\farcm5$, we smooth the map with a Gaussian filter having a full width at half-maximum of 2′ (2 pixels). Figure 1 shows a contour plot of such a map. To derive the IPC surface brightness profile, we bin the count rate map into circular azimuthal rings 1′ in width. We azimuthally average the count rates in each ring to generate the count rate as a function of projected radius.

Before we study the simulated observations we should first discuss the issue of absorption. In real clusters the amount of absorption is important since low-energy X-ray emission is preferentially absorbed. Besides decreasing the overall observed count rates, absorption also changes the shape of the emission spectrum. We have not included absorption in generating the simulated *EXOSAT* and IPC data. This is for the following reasons. In the case of *EXOSAT*, the spectra that we consider cover a range in energy from 1 to 10 keV. As an example, if a rather high column density of 10^{21} cm^{-2} were present, absorption would reduce the flux at 1 and 2 keV to ~ 0.8 and ~ 0.96, respectively, of the unabsorbed values (using the photoionization cross sections of Morrison & McCammon 1983). Since the photoionization cross section goes roughly as (energy)$^{-3}$, there is negligible absorption over most of the energy range under consideration. The addition of absorption simply reduces the emission at the lowest energies somewhat. In addition, the comparison of our simulated *EXOSAT* spectrum to that of real clusters is done by comparing the quality of isothermal fits to the respective data. An observer who is fitting data from real clusters may have knowledge of the column density from other measurements, such as H I observations. In this case, he would make the fit assuming the given column density. We too could say that we know that there is no absorption in our cluster and then make a fit with that assumption. In this sense, any absorption that we could have put in when we produced the simulated spectrum could be trivially accounted for during the fitting process.

Real *EXOSAT* observations, however, also allow the determination of the column density from the fit itself (Edge 1989). It is generally useful to check if the values derived in this way are consistent with the values derived from observations of the H I column density. A similar procedure can be carried out with our simulated cluster. An observer viewing our cluster would not know a priori without other information that there is no absorption. He would let the fit to the spectrum determine the column density. Therefore, in the subsequent fitting, we allow the column density to vary as a parameter of the fit. The results of this fitting also allows us to determine if estimates of the absorption from X-ray spectral information for real clusters are reliable.

In the case of the IPC, spectral information from this instrument for real clusters have in general not been of a high enough quality to allow stringent limits to be placed on the absorption. Work with the IPC generally assumes a value obtained by other means. As observers who again do not know the column density to the simulated cluster, we make fits to the imaging data by adopting a value taken from another source, in this case the fits to the simulated *EXOSAT* data.

The points in Figure 6 show the *EXOSAT* spectra of the simulated cluster generated in the manner described above. These spectra correspond to the cluster being viewed down the x-axis as defined by KW. Spectra from other projections appear similar and are not plotted. The Poisson errors are less than 1% and are smaller than the size of the dots in the figure. The upper spectrum includes emission from the entire cluster

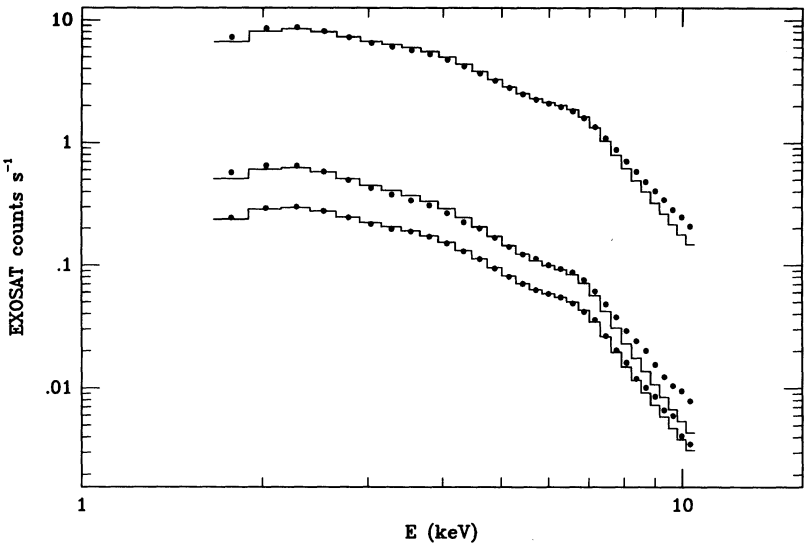

FIG. 6.—Dots show the simulated *EXOSAT* spectra. The Poisson error bars are smaller than the size of the dots. The top curve corresponds to the spectrum when the entire cluster is observed (case 1), the middle curve corresponds to the spectrum when an inner sphere of radius 70 kpc is excluded (case 2), and the lower curve corresponds to the spectrum when all the incorrectly modeled regions of the simulation are removed (case 3). The solid histograms give the best-fit isothermal spectra.

(case 1), the middle spectrum only includes emission outside the central 70 kpc (case 2), and the lower spectrum excludes the emission from all the unrealistic parts of the cluster (case 3). The emission from the central 70 kpc accounts for a large fraction of the emission detected by *EXOSAT* as shown by the large displacement of the top two curves in Figure 6. The smaller difference between the middle and bottom curves implies that the emission from the other galaxies and the projected group is much less significant. Remember that it is most appropriate to compare the lower spectrum directly with observations. Qualitatively, the features of all the spectra are similar to the spectra of actual clusters (Edge 1989). The overall shapes are similar to real spectra and the bump at around 7 keV, which is due to the complex of Fe K lines, is prominent. In a more detailed sense, however, a significant difference exists between the top two spectra and the spectra from real clusters. This difference is easily seen if we reproduce the typical procedure of making isothermal fits to the spectra.

It is generally found that the *EXOSAT* spectra of real clusters can be well fitted by isothermal models (Edge 1989). To determine whether our simulated spectra can be similarly fitted, we assume an isothermal model that has one-half solar metal abundances. In spectral fitting to real clusters the abundances of the metals are not known a priori but are determined by the fitting procedure itself from the equivalent width of the 7 keV Fe K lines for iron and then are just inferred for most of the other elements. We avoid this aspect of the fitting procedure to isolate the effects of temperature on the fit. As discussed above, the column density of absorbing gas is allowed to vary as a parameter of the fit. The photoionization cross sections are from Morrison & McCammon (1983).

The solid histograms in Figure 6 are the isothermal fits to the simulated data. We do not obtain a formally good fit for any of the spectra. Recall that the error bars are much smaller than the size of the dots. At large energies the fit is deficient in counts in all the spectra, but in the top two spectra even at lower energies the shape of the fit is not consistent with that of the data. Because we only include Poisson noise in estimating the errors, it is possible that fits to our simulated data would be considered acceptable if we were to include additional errors due to background subtraction and instrumental considerations. Real *EXOSAT* spectra have these sources of error, and the larger errors could hide a poor isothermal fit to the data.

We investigate this possibility by examining the estimated errors in real *EXOSAT* data where all the previously mentioned effects are included (see chapter 4 of Edge 1989). The error bars are not much bigger than the purely statistical errors except at the highest energies where uncertainties in the background subtraction significantly increase the errors. For example, NGC 1275 in Perseus is roughly at the same distance as our simulated cluster and has a somewhat lower mass accretion rate of 270 $M_\odot$ yr^{-1}, so we use it to compare with our simulated cluster. In this object, the total errors in the *EXOSAT* data at low energies remain 1% or 2%. This amount of error would still lie within the size of the dots in Figure 6 suggesting that the isothermal fit to the top two spectra would remain poor even if realistic error bars were included. However, when these larger and more realistic errors are included in the isothermal fits to the lower spectrum, particularly at higher energies, the fit is formally acceptable. Because the lower spectrum (case 3) best represents the realistic emission from the simulated cluster, the temperature structure of the intracluster gas in the simulated cluster is consistent with *EXOSAT* spectral observations of real clusters. Also, since the simulated *EXOSAT* spectrum can be fitted by an isothermal model even though the intracluster gas is not isothermal, a comparable degree of nonisothermality in real intracluster gas could be hidden despite the good fit of the isothermal models.

In Table 1 we list the best-fit isothermal temperatures to the simulated cluster spectra. The first column specifies the axis from which we view the cluster. Although the axes are specified to be the same as those used in KW, they can be regarded as three random orientations and thus indicate the sensitivity of the temperature determinations to the orientation of the cluster. The specification "no center" indicates that the spectrum was computed without the central emission excess (case 2), and "no galaxies" indicates that all the suspect regions have been removed (case 3). The derived isothermal temperatures

TABLE 1

EXOSAT BEST-FIT TEMPERATURES

Projection	Derived Temperature (10^7K)
x-axis	4.50
x-axis (no center)	3.06
x-axis (no galaxies)	3.58
y-axis	4.08
y-axis (no center)	3.59
y-axis (no galaxies)	3.60
z-axis	4.37
z-axis (no center)	3.57
z-axis (no galaxies)	3.62

NOTE.—The first column gives the direction in which the simulated cluster is viewed and when the emission from the central region or all "galaxies" have been excluded. The best-fit temperatures resulting from isothermal fits to simulated *EXOSAT* observations are given in the second column.

seem consistent with emission-weighted averages of the temperature within the *EXOSAT* field when compared to the known temperature profile shown in Figure 3*a*. Furthermore, variations in the derived temperature due to different projections are ~10% and are only ~1% when the unrealistic emission is removed (case 3). Therefore, we can most likely regard an uncertainty of 10% as an upper bound for most real clusters if we assume that real clusters are at least as spherical as our simulated cluster. This is a good assumption for many clusters. For example, the X-ray isophotes of the gas around M87 are more circular than the isophotes in Figure 1 (Fabricant & Gorenstein 1983).

In all cases listed in Table 1, the best-fit column density of absorbing gas is zero, the actual value. This implies that the changes in the low-energy part of the spectrum due to any absorption are sufficient to provide a robust estimation of the column density. We also assume no column density in the subsequent IPC analysis.

In Figure 7 we plot the IPC surface brightness profile for the simulated cluster viewed along the *x*-axis. The surface brightness profiles from the other projections look similar and are not shown. The statistical errors are small, and their associated error bars fall within the size of the dots at small radii where the errors are less than 1% and are about the size of the dots at large radii, ~5%. It is evident from the figure that the three innermost data points fall within the central X-ray cusp. Compared to the XD clusters observed by Jones & Forman (1984), the central X-ray cusp is unrealistically large, further confirming the unrealistic nature of the simulation's central region. Outside this central region, the surface brightness profile looks like a generic centrally flattened power law with a core radius of about 250 kpc. The surface brightness exceeds a power law at the five outermost points owing to contamination by incorrectly modeled galactic gas.

We replicate the fitting process usually applied to IPC data (Fabricant & Gorenstein 1983; Jones & Forman 1984) to compare the simulated IPC surface brightness profile to actual data. We assume that the density profile follows equation (2) and that the gas is isothermal with the temperature given by the isothermal fit to the *EXOSAT* spectrum. With these assumptions, the model surface brightness profile is computed assuming the atomic emissivities of Raymond (1989). We compare the model to the simulated data and adjust the parameters of the density profile (n_0, a, and β) to give the best possible fit. When doing this fit, we exclude the three innermost data points, consistent with the procedures of Jones & Forman (1984). These inner points are excluded because the simulated cluster is classified as an XD cluster. Real XD clusters cannot be fitted by "β"-models at small radii because of the central X-ray cusp. Observers use the amount of central emission in excess of the model to determine the amount of cooling present in the center of the cluster. We also exclude the five outermost points from the fit owing to the contamination by the two outer "galaxies." The best fit is plotted as the solid line in Figure 7, and Table 2 lists the best-fit parameters.

The quality of the fit is somewhat poor, particularly in the

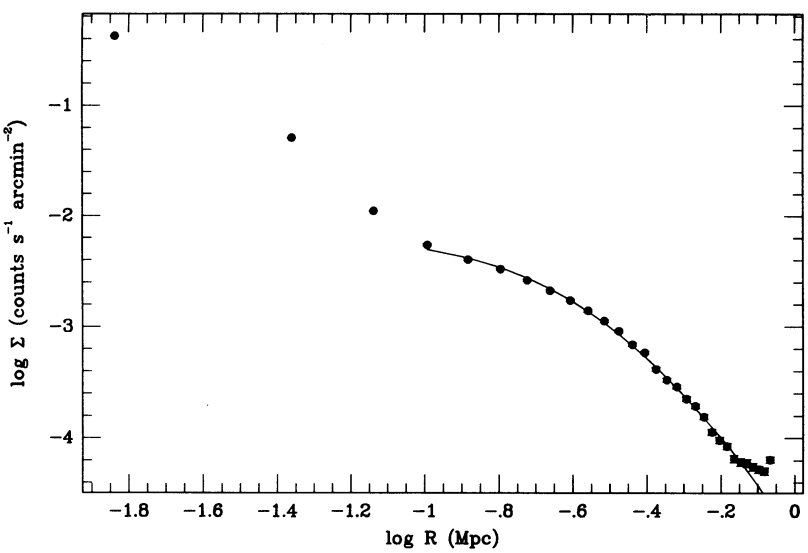

FIG. 7.—Dots show the simulated IPC X-ray surface brightness profile when the counts are binned into circular annuli 1′ in width. At small radii the Poisson error bars are smaller than the size of the dots, and at large radii the Poisson error bars are comparable to the size of the dots. The solid line shows the best-fit isothermal "β" model.

TABLE 2

IPC BEST-FIT PARAMETERS (ISOTHERMAL)

Projection	n_0 ($\times 10^{-3}$ cm^{-3})	a (kpc)	β
x-axis	2.05	260	0.807
x-axis (no center)	2.04	260	0.807
y-axis	2.48	190	0.673
y-axis (no center)	2.47	189	0.673
z-axis	1.88	278	0.813
z-axis (no center)	1.87	278	0.813

NOTE.—We list in cols. (2)–(4) the best-fit parameters for the density profile (eq. [2]) from the fit to simulated IPC observations. The gas is assumed to be isothermal for the fit. The first column indicates the direction in which the clusters are viewed.

inner regions. As in the *EXOSAT* observations, however, real data have additional errors associated with background subtraction and instrumental effects. For example, in their work on M87, Fabricant & Gorenstein (1983) add a 6% error in quadrature to the statistical errors to account for instrumental gain and vignetting correction uncertainties. A further background subtraction error is also included which significantly affects the outermost points. As with the M87 data, the instrumental error would dominate the statistical errors in our simulated observation and would make our fit to the data acceptable. Therefore, we can fit the IPC surface brightness of our simulated cluster using the standard parameterization of the density when we include realistic errors.

In Table 2 we tabulate the best-fit parameters to the simulated IPC data. The column marked "projection" indicates the viewing direction and "no center" indicates that the fit to the simulated IPC data is made assuming the isothermal temperature derived from the simulated *EXOSAT* spectrum that excluded the emission from the incorrectly modeled central region (case 2). The next three columns give the values of the best-fit parameters in the different cases. The last column simply is the derived value of the standard β parameter. In the isothermal model of Cavaliere & Fusco-Femiano (1976), β is equal to the ratio of the kinetic energy in the galaxies to the thermal energy in the gas. Of course, since our gas is not isothermal, β does not have this exact physical interpretation, but we simply regard it as a parameter of the fit. When this fit is done assuming that the gas is isothermal, the value of β is fixed by the slope of the surface brightness profile at large radius. This is because the density of equation (2) implies a surface brightness profile given by

$$S(r) = S_0\left[1 + \left(\frac{r}{a}\right)^2\right]^{-3\beta+1/2}, \qquad (8)$$

where S and S_0 are given in units of ergs s^{-1} cm^{-2} arcmin^{-2}. Since the fits are insensitive to the assumed temperature, we do not bother to tabulate the fits using the temperatures derived when all the unrealistic regions of the cluster are removed (case 3). This temperature insensitivity also implies that our X-ray surface brightness fits are not affected by the unrealistic regions of the simulation.

When we compare our best-fit parameters to those of the clusters in the sample of Jones & Forman (1984), we find several interesting things. Because our cluster has a relatively small mass, we only compare it to the smallest clusters in the sample, namely A194, A262, A400, A576, A1060, and SC 0559 − 40. A194 and SC 0559 − 40 are considered irregular clusters so we will not consider them. Of the remaining clusters, A262, A576, and A1060 are classified as XD clusters, so we use them to compare with the simulated cluster. The simulated cluster has values of β and central density (n_0) comparable to the observed values for these clusters. The core radii for the observed clusters tend to be somewhat smaller than that of the simulated cluster by about a factor of 2, but the range in the observed core radii is somewhat large. Since our simulated cluster is rather small, we can also ask how our results compare with a sample of smaller clusters. Such a sample has been observed by Kriss et al. (1983), and again our parameters agree quite well with those derived from real clusters.

In Figure 8 we show the derived density profiles for three different projections. The solid line corresponds to the derived density when the cluster is viewed along the x-axis. The "no center" fits are essentially identical to these determinations made with the cluster center included. The dotted line and the short dashed lines correspond to the derived density profiles when the cluster is viewed along the y- and z-axes, respectively. As with the temperature determinations, the density profiles are not very different when observed from three different directions. When the cluster is viewed along the y-axis the slope at large radii is slightly different but only significantly so at radii larger than 1 Mpc where we have not constrained the fits. Therefore, despite the elliptical X-ray isophotes, the derived spherically averaged density profiles are almost independent of the viewing angle.

Since we observe a simulation, knowing the actual density allows us to determine the accuracy of the fitting procedure. The dots in Figure 8 show the actual spherically averaged density profile (simply reproduced from Fig. 3*b*). At the radii where we fit the "data," the density profile is accurately determined. Beyond 1 Mpc, the derived profiles deviate from the known density profile, but again this is expected since we did not include data from these large radii in our model fits. Finally, we check that the derived density profile is not significantly changed by assuming a different temperature when fitting the IPC data. In Table 3 we list the derived parameters for the density profiles when we make fits using the actual temperature profile. The derived density profiles are not significantly changed since the emissivity over the IPC band at these temperatures is almost independent of temperature.

4. MASS PROFILES

Given the density profiles derived from fitting the simulated IPC observations and using the isothermal temperatures derived from the *EXOSAT* spectral fits, we can determine the

TABLE 3

IPC BEST-FIT PARAMETERS (NONISOTHERMAL)

Projection	n_0 ($\times 10^{-3}$ cm^{-3})	a (kpc)	β
x-axis	2.05	264	0.827
y-axis	2.48	195	0.693
z-axis	1.90	276	0.820

NOTE.—We list in cols. (2)–(4) the best-fit parameters for the density profile (eq. [2]) from fits to simulated IPC observations. The actual temperature profile of the gas is assumed for the fit. The first column gives the direction in which the simulated cluster is viewed.

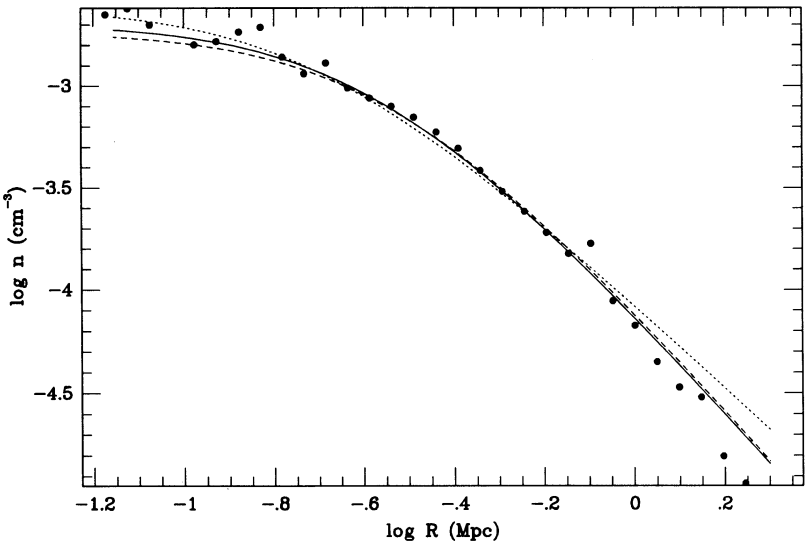

FIG. 8.—Density profiles that result from isothermal fits to the IPC surface brightness profiles. The three plots correspond to the derived density when the cluster is viewed along x-, y-, and z-axes of Katz & White (1993). The solid line corresponds to the x-axis, the dotted line corresponds to the y-axis, and the dashed line corresponds to the z-axis. The dots show the actual density.

mass profile. Assuming hydrostatic equilibrium,

$$M(r) = -\frac{kT}{G\mu m_p}\left(\frac{d\log\rho}{d\log r} + \frac{d\log T}{d\log r}\right)r\,, \qquad (9)$$

where μ is the mean molecular weight of the gas and m_p is the proton mass. An observer could not directly test, as we do here, whether the cluster gas is in hydrostatic equilibrium. An observer would simply make certain that the cooling time was longer than the dynamical time at the radii of interest. If such a check were performed on the simulated cluster, it would lead an observer to conclude that the cluster was in hydrostatic equilibrium (§ 2).

The mass profiles derived from the simulated observations are plotted in Figure 9. The solid line corresponds to the cluster being viewed along the x-axis, the dotted line corresponds to the y-axis, and the short dashed line corresponds to the z-axis. The dots plot the actual spherically averaged mass profile of the simulation. In these mass determinations, we use the isothermal temperatures from fits to the spectra generated when all the unrealistic regions of the simulated cluster are removed (case 3). Since we assume the gas is isothermal, the temperature derivative term in equation (9) vanishes, and the mass is just linearly proportional to the temperature. A different choice for the temperature would simply shift the curves by a constant factor. The derived masses are not sensitive to the viewing angle. The mass profiles derived from the different projections agree within 25%. At large radii, the y projection yields the lowest mass estimate because the y projection derived slope for the density profile is the smallest, and at small

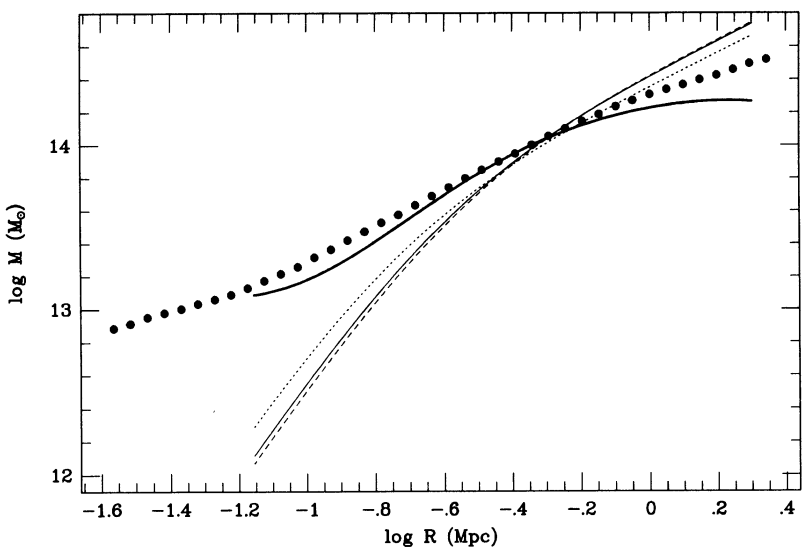

FIG. 9.—Actual and derived cluster mass profiles assuming the equation of hydrostatic equilibrium. Assuming that the gas is isothermal, the solid line corresponds to the x projection, the dotted line corresponds to the y projection, and the dashed line corresponds to the z projection. The heavy solid line corresponds to the mass derived when the actual temperature profile is used. The dots give the actual total mass of the cluster.

radii it yields the largest mass estimate because the derived density slope is the largest.

In all three projections, the derived profiles disagree with the actual mass profiles both at small and large radii. Within the radii where we constrained the density profiles and the temperature, that is, between 100 kpc and 1 Mpc, the largest discrepancy is a factor of 6 deficit at 100 kpc. Between 200 kpc and 2 Mpc, however, the discrepancy is less than a factor of 2. It is easy to understand why the slopes of the derived mass profiles are too steep by examining equation (9). The mass determination strongly depends on the temperature profile. The assumption of isothermality when the gas is not isothermal leads to the systematic difference in slope. We further discuss this below. We conclude, however, that if the nonisothermality and ellipticity of the simulated cluster represents real clusters, cluster masses cannot be determined to better than a factor of 2 when isothermality is assumed. The masses would be underestimated at small radii and overestimated at large radii. If, however, an observer were able to obtain additional information about the temperature profile, for example, from spectral observations, it might be possible to improve the mass determination.

We investigate this by using the actual temperature profile to derive the cluster mass using equation (9). Of course, real spectral observations of a cluster probably would not yield the exact temperature profile so this represents a best case scenario. Since our temperature profile is bumpy (see Fig. 3*a*) and we have to differentiate it, we fit it to a cubic polynomial first, excluding the points interior to about 10 kpc. Using this temperature profile and the density derived from the simulated IPC data also using the actual temperature profile (the parameters of Table 3), we determine the mass using equation (9). We plot the result in Figure 9 as the heavy solid line. As expected, the mass determination is greatly improved using the actual temperature profile; inside 1 Mpc the derived masses and the actual masses agree within 25%.

Outside of 1 Mpc, however, the derived mass falls increasingly below the actual mass, reaching a factor of 1.5 deficit at 1.6 Mpc. Part of this difference is due to the fact that the derived density profile used to determine the mass has a shallower slope than the actual density profile at these radii (see Fig. 8). When we use the actual density profile in the mass determination, the error decreases to a factor of 1.2. We attribute the remaining discrepancy to the assumption of spherical symmetry and to violations of hydrostatic equilibrium. Recall that at the large radii under consideration, the velocity-dependent terms of the Euler equation become more important since the magnitude of both the pressure and gravity terms are decreasing (see Fig. 2). Since the total mass is underestimated and the gas mass is determined correctly, the relative amount of baryonic material appears to increase at large radii. Although this is outside the simulated cluster's virial radius of $\sim$900 kpc, a similar effect may contribute to the apparent preponderance of baryonic material at large radii in recent cluster observations. However, we still conclude that the greatest sources of error in determining cluster masses using X-ray data, at least within the virial radius, are associated with errors in the assumed temperature profile.

An alternative to isothermal modeling of the cluster gas is the assumption of a polytropic law for the temperature distribution (e.g., Cowie, Henriksen, & Mushotzky 1987; Hughes et al. 1988). Since the actual temperature in the simulation is closer to a polytropic profile than to an isothermal profile (see Fig. 3*a*), we expect that mass estimates from polytropic modeling of the simulated cluster would be better than from the above isothermal modeling. However, there is no guarantee that polytropic modeling applied to real clusters would give a better estimate than isothermal modeling because of the uncertainty in the temperature profiles.

One more point regarding the derived mass profiles concerns a proposed solution to the "β problem." Historically, this "problem" is simply the mismatch in the results of two different ways in which the β of equation (2) can be evaluated. The problem only exists in the context of the isothermal "β"-models of Cavaliere & Fusco-Femiano (1976) where it is assumed that the gas and galaxy distributions are both isothermal and static, and that the galaxies and gas sit in a common potential. In this case, β can be evaluated by fitting the density of equation (2) to imaging data, as we have done in § 3 for our simulated IPC observations. The value of β is also equal to the ratio of the energy in galaxies to the thermal energy of the gas. The former can be determined from galaxy velocity dispersion measurements and the latter from isothermal fits to spectral data. Fits to imaging data generally give $\beta \sim 0.7$ (Jones & Forman 1984), whereas the spectral method generally gives higher values of $\sim$1.2 (Jones & Forman 1984; Mushotzky 1984). It has since been realized that the difference in the two values may simply be due to observational uncertainties. Newly derived values from the spectral method are more consistent with the previous imaging values (Edge & Stewart 1991; Lubin & Bahcall 1993). Prior to this observational discovery, Evrard (1990) attempted to understand the "β problem" with simulations. He found that a discrepancy in the values derived from the two methods arose because of an extra pressure generated by the incomplete thermalization of the gas in his simulation. This extra pressure also resulted in the systematic underestimate of the mass at all radii when the hydrostatic method was used (see his Fig. 12). From the heavy solid line of Figure 9, we see that there is no such offset in our estimates except at large radius where the reasons for the discrepancy are known from the previous paragraph.

We cannot address issues directly related to the "β problem" here since we have too few galaxies to allow an estimate of the galaxy velocity dispersions. Future simulations with sufficient numbers of galaxies not only will allow an understanding of the "β problem," but also will address such questions as whether the galaxies trace the total mass. This issue is uncertain since Buote & Canizares (1992) show that the galaxy distribution is less round than the dark matter distribution, whereas Lubin & Bahcall (1993) claim that the galaxies do indeed trace the dark matter distribution.

5. CONCLUSIONS

We carefully analyzed the properties of the intracluster gas in the simulation of Katz & White (1993) and reached the following conclusions.

1. By evaluating the terms in the Euler equation, we find that the velocity-dependent terms are much smaller than the gas pressure and gravitational terms, demonstrating that the intracluster gas is in hydrostatic equilibrium.

2. By examining the values of the fluid variables and relevant timescales, we show that within a radius of $\sim$400 kpc, gas flows subsonically toward the central "galaxy." Inside $\sim$100 kpc, somewhat outside the actual cooling radius, this flow is in a steady state. Since the cooling time is longer than a Hubble time everywhere except within the central 50 kpc, the flow is

not regulated by local cooling. The flow rate is controlled instead by the amount of gas required to accrete into the center to maintain the extremely high central emission. Therefore, a cooling flow cluster arises naturally in the standard CDM cosmological model considered here.

3. By "observing" the simulated cluster with the *EXOSAT* ME detector we find that an isothermal model gives a good fit to the simulated cluster spectrum, consistent with *EXOSAT* ME observations of real clusters. In addition, since the intracluster gas in the simulated cluster is not isothermal, a certain degree of nonisothermality could be hidden in *EXOSAT* spectra. The column density of absorbing gas toward a given cluster can be accurately determined from spectral fitting.

4. By also "observing" the simulated cluster with the *Einstein* IPC we find that the simulated surface brightness profiles fit the standard "β" model profile as well as real clusters. The derived parameters of the fit (central density, core radius, and slope) are consistent with the observed values of real clusters in the surveys of Jones & Forman (1984) and Kriss et al. (1983).

5. We simulate the standard method for determining cluster mass profiles using X-ray data assuming temperatures derived from the isothermal fits to the simulated *EXOSAT* spectrum and density profiles derived from fits to the simulated IPC surface brightness profile. These mass estimates are in error by as much as a factor of 6, although at most radii the error is a factor of ~ 2. If the actual temperature profile is used to determine the mass instead of an isothermal value, the accuracy is improved to better than 25%, at least within the virial radius. The greatest source of error in cluster mass estimates is due to inaccuracies in the temperature determination. The remaining uncertainties due to the lack of spherical symmetry and violations of hydrostatic equilibrium are less than 25% at these radii. The conclusion that dark matter must make up most of cluster masses is not in doubt due to uncertainties in cluster mass estimates. We note that our conclusions are consistent with those of Fabricant, Rybicki, & Gorenstein (1984).

This paper is based on work done by J.C.T. in partial fulfillment of the requirements for the Ph.D. at Massachusetts Institute of Technology. We thank Ed Ajhar, Dan Fabricant, Eric Linder, Gene Magnier, Mark Metzger, and Bob Rutledge for useful discussions. J. C. T. was supported by NASA grants NAG 5-1220 and NAG 5-1355, NSF grant AST 90-01762, and an NRC associateship. N.K. was supported by a Hubble fellowship.

REFERENCES

Arnaud, K. A. 1988, in Cooling Flows in Clusters of Galaxies, ed. A. C. Fabian (Dordrecht: Kluwer), 31
Bertschinger, E. 1989, ApJ, 340, 666
———. 1993, Ann. NY Acad. Sci., 688, 297
Buote, D. A., & Canizares, C. R. 1992, ApJ, 400, 385
Canizares, C. R., Markert, T. H., & Donahue, M. E. 1988, in Cooling Flows in Clusters of Galaxies, ed. A. C. Fabian (Dordrecht: Kluwer), 63
Cavaliere, A., & Fusco-Femiano, R. 1976, A&A, 49, 137
Cen, R., & Ostriker, J. P. 1992, ApJ, 399, L113
Cowie, L. L., Henriksen, M., & Mushotzky, R. 1987, ApJ, 317, 593
Edge, A. C. 1989, Ph.D. thesis, Univ. Leicester
Edge, A. C., & Stewart, G. C. 1991, MNRAS, 252, 428
Edge, A. C., Stewart, G. C., & Smith, A. 1988, in Hot Thin Plasmas in Astrophysics, ed. R. Pallavicini (Dordrecht: Kluwer), 335
Edgar, R. J., & Chevalier, R. A. 1986, ApJ, 310, L27
Evrard, A. E. 1990, ApJ, 363, 349
Evrard, A. E., Summers, F. J., & Davis, M. 1994, ApJ, in press
Fabian, A. C., Nulsen, P. E. J., & Canizares, C. R. 1984, Nature, 310, 733
Fabricant, D., & Gorenstein, P. 1983, ApJ, 267, 535
Fabricant, D., Lecar, M., & Gorenstein, P. 1980, ApJ, 241, 552
Fabricant, D., Rybicki, G., & Gorenstein, P. 1984, ApJ, 286, 186
Frenk, C. S., White, S. D. M., Efstathiou, G., & Davis, M. 1990, ApJ, 351, 10
Gelb, J. M. 1992, Ph.D. thesis, Massachusetts Institute of Technology
Giacconi, R., et al. 1979, ApJ, 230, 540
Heisler, J., Tremaine, S., & Bahcall, J. N. 1985, ApJ, 298, 8
Hernquist, L., & Katz, N. 1989, ApJS, 70, 419
Hughes, J. P., Yamashita, K., Okumura, Y., Tsunemi, H., & Matsuoka, M. 1988, ApJ, 327, 615
Jones, C., & Forman, W. 1984, ApJ, 276, 38
Katz, N., & Gunn, J. E. 1991, ApJ, 377, 365
Katz, N., Hernquist, L., & Weinberg, D. H. 1992, ApJ, 399, L109
Katz, N., & White, S. D. M. 1993, ApJ, 412, 455 (KW)
Koyama, K., Takano, S., & Tawara, Y. 1991, Nature, 350, 135
Kriss, G. A., Cioffi, D. F., & Canizares, C. R. 1983, ApJ, 272, 439
Lubin, L., & Bahcall, N. 1993, preprint
Morrison, R., & McCammon, D. 1983, ApJ, 270, 119
Mushotzky, R. F. 1984, Phy. Scripta, T7, 157
Ostriker, J. P. 1993, ARA&A, in press
Perrenod, S. C. 1978, ApJ, 226, 566
Raymond, J. C. 1989, private communication
Sarazin, C. L. 1988, X-Ray Emission from Clusters of Galaxies (Cambridge: Cambridge Univ. Press)
Stewart, G. C., Canizares, C. R., Fabian, A. C., & Nulsen, P. E. J. 1984, ApJ, 278, 536
Tsai, J. C. 1993, ApJ, submitted
———. 1994, ApJ, in press
Thomas, P. A., & Couchman, H. M. P. 1992, MNRAS, 257, 11
Tyson, J. A. 1991 in After the First Three Minutes, ed. S. S., Holt, V., Trimble & C. Bennett, (New York: American Institute of Physics), 437
Tyson, J. A., Valdes, F., Jarvis, J. F., & Mills, A. P. 1984, ApJ, 281, L59
Tyson, J. A., Valdes, F., & Wenk, R. A. 1990, ApJ, 349, L1